

Multi-epoch X-ray observations of the Seyfert 1.2 galaxy Mrk 79: bulk motion of the illuminating X-ray source

L. C. Gallo,^{1*} G. Miniutti,² J. M. Miller,³ L. W. Brenneman,⁴ A. C. Fabian,⁵ M. Guainazzi⁶ and C. S. Reynolds⁷

¹Department of Astronomy and Physics, Saint Mary's University, 923 Robie Street, Halifax, NS B3H 3C3, Canada

²Centro de Astrobiología (CSIC-INTA), Departamento de Astrofísica, LAEFF, PO Box 78, Villanueva de la Cañada, E-28691 Madrid, Spain

³Department of Astronomy, University of Michigan, 500 Church Street, Ann Arbor, MI 48109, USA

⁴Harvard-Smithsonian Center for Astrophysics, MS 67, 60 Garden Street, Cambridge, MA 01238, USA

⁵Institute of Astronomy, University of Cambridge, Madingley Road, Cambridge CB3 0HA

⁶European Space Astronomy Centre of ESA, Apartado 50727, E-28080 Madrid, Spain

⁷Department of Astronomy and the Maryland Astronomy Center for Theory and Computation, University of Maryland, College Park, MD 20742, USA

Accepted 2010 September 13. Received 2010 September 7; in original form 2010 June 23

ABSTRACT

Multi-epoch X-ray spectroscopy (0.3–25 keV) of the Seyfert 1.2 galaxy Mrk 79 (UGC 3973) spanning nearly 8 yr and a factor of 3 in broad-band flux are analysed. The data are obtained at seven epochs with either *XMM-Newton* or *Suzaku*. Comparison with contemporaneous *RXTE* monitoring indicates that all flux states of Mrk 79 are represented by the data. The spectra are fitted in a self-consistent manner adopting a power law and ionized reflection to describe the broad-band continuum. Modification of the spectra by a distant photoionized medium, seen predominantly in emission, is also included. Under the assumption that the inner disc is at the innermost stable circular orbit, our blurred reflection models give a spin of $a = 0.7 \pm 0.1$. The reflection component in each spectrum is weaker than that predicted by simple reflection models. If the illuminating X-ray emission is produced by flares above the disc that move at mildly relativistic velocities, however, diminished reflection is expected. Light bending due to strong gravity near black holes can influence how the illuminating and reflected fluxes are observed; variations in Mrk 79 do not suggest that light bending is important in this source.

Key words: galaxies: active – galaxies: individual: Mrk 79 – galaxies: individual: UGC 3973 – galaxies: nuclei – X-rays: galaxies.

1 INTRODUCTION

The X-ray spectra of Type I active galactic nuclei (AGN) can exhibit significant variability from one epoch to the next, and the general spectral shape can normally be associated with the flux state of the AGN. For example, in the low-flux state the power-law emission above ~ 2 keV is flatter and the excess above the power law at energies of $\lesssim 2$ keV (i.e. the so-called soft excess) is relatively stronger than in the high-flux state. In addition, the 2–10 keV band often displays complexity in the form of spectral curvature or spectral drops in the low-flux state (e.g. Gallo et al. 2004; Grupe et al. 2008; Bachev et al. 2009). However, defining the flux ‘state’ for AGN is more complicated than for black hole binaries because the characteristic time-scales are much longer in AGN. Long-term monitoring (i.e. years) is generally required to properly determine flux states. Gallo (2006) even suggested that the hypothetical

UV-to-X-ray slope (α_{ox}) may be better suited for defining the X-ray low state rather than X-ray flux alone. Consequently, it is challenging to gain understanding of a particular system from single-epoch observation without information on its typical variability behaviour.

An advantage of multi-epoch modelling is that model parameters that vary on different characteristic time-scales can be examined and constrained accordingly. While black hole spin, disc inclination and elemental abundances are not expected to change, power-law spectral slopes can vary on day-long scales (perhaps more rapidly) (e.g. Iwasawa et al. 2010; Sobolewska & Papadakis 2009), and the inner disc ionization parameter and the absorber covering fraction have been suggested to vary rapidly (10^3 – 4 s) (Ponti et al. 2006, 2010; Risaliti et al. 2009).

In this work, multi-epoch X-ray observations of the Seyfert 1.2 galaxy Mrk 79 (UGC 3973; $z = 0.022189$) are examined to study the nature of its X-ray emission and variability. Mrk 79 is well studied in the optical, benefiting from efforts to measure its black hole mass by reverberation mapping (e.g. Peterson et al. 2004). However, despite being relatively bright ($\gtrsim 10^{-11}$ erg cm $^{-2}$ s $^{-1}$ between

*E-mail: lgallo@ap.smu.ca

Table 1. Mrk 79 observation log. Each data set will be referred to in the paper by the identifier in Column 1. The observatory used to obtain the data and the observation ID are given in Columns 2 and 3, respectively. The start date and duration of the observation are shown in Columns 4 and 5, respectively. Column 6 shows the GTI for each observation. The *Suzaku* exposure is combined for all three XIS. Column 7 provides the total source counts in the 0.3–12 keV band (0.5–10 keV for *Suzaku*).

(1) Observation	(2) Observatory	(3) Observation ID	(4) Start date (yr.mm.dd)	(5) Duration (s)	(6) Exposure (s)	(7) Counts
XMM1	<i>XMM–Newton</i>	0103860801	2000.10.09	6904	1680	20827
XMM2	<i>XMM–Newton</i>	0103862101	2001.04.26	6935	3590	21454
XMM3	<i>XMM–Newton</i>	0400070201	2006.09.30	24 000	14 411	238 259
XMM4	<i>XMM–Newton</i>	0400070301	2006.11.01	21 500	13 993	150 349
XMM5	<i>XMM–Newton</i>	0400070401	2007.03.19	21 500	13 992	156 980
SUZ1	<i>Suzaku</i>	702044010	2007.04.03	160 017	251 127 (XIS0+XIS1+XIS3)	202 872
XMM6	<i>XMM–Newton</i>	0502091301	2008.04.27	90 400	58 262	136 940

0.5 and 10 keV) Mrk 79 is poorly studied in the X-rays. Snap-shot observations of Mrk 79 were done in 2000 and 2001 with *XMM–Newton*, marking the first time the spectrum above 2 keV was analysed (Gallo et al. 2005, 2006). The observations revealed a soft excess, possible warm absorption and a slightly broadened Fe $K\alpha$ emission line. Gallo et al. (2005) reported a possible 8-keV emission feature in the 2001 observation, but this is not confirmed with the deeper observations presented here.

In the following section, the observations and data reduction are described. In Section 3, the data sets are examined and characterized. The reflection grating spectrometer (RGS) spectrum is analysed in Section 4 to understand the nature of the ionized plasma. The high-energy spectrum above 3 keV is examined in Section 5. A self-consistent model simultaneously describing all the data is presented in Section 6. Our results and conclusion are discussed in Sections 7 and 8, respectively.

2 OBSERVATIONS AND DATA REDUCTION

Mrk 79 was observed with *XMM–Newton* (Jansen et al. 2001) on six occasions between 2000 and 2008 and once in 2007 with *Suzaku* (Mitsuda et al. 2007). A summary of the observations is provided in Table 1 along with the nomenclature we adopt throughout this work.

The EPIC pn (Strüder et al. 2001) and MOS (MOS1 and MOS2; Turner et al. 2001) cameras were operated in small-window mode with the medium filter in place for all the observations except XMM6 when the thin filter was used. RGS1 and RGS2 (den Herder et al. 2001) also collected data during this time, as did the optical monitor (OM; Mason et al. 2001).

The *XMM–Newton* Observation Data Files from all observations were processed to produce calibrated event lists using the *XMM–Newton* Science Analysis System (SAS v9.0.0). Unwanted hot, dead or flickering pixels were removed as were events due to electronic noise. Event energies were corrected for charge-transfer inefficiencies. EPIC response matrices were generated using the SAS tasks *arfgen* and *rmfgen*. Light curves were extracted from these event lists to search for periods of high background flaring. Significant flaring was detected during the final ~ 18 ks of XMM6, and data during these periods have been neglected. The total amount of good pn exposure is listed in Table 1. Source photons were extracted from a circular region of 35 arcsec across and centred on the source. The background photons were extracted from an off-source region on the same CCD. Single and double events were selected for the pn

detector, and single-quadruple events were selected for the MOS. The MOS and pn data at each epoch are compared for consistency and determined to be in agreement within known uncertainties (Guainazzi 2010). For simplicity in analysis and presentation, only the pn data are discussed here.

The RGS spectra were extracted using the SAS task *rgsproc* and response matrices were generated using *rgsrmfgen*. The OM operated in imaging mode with various filters in place at different epochs. However, an ultraviolet image was obtained at every epoch in either the *UVW1* (2450–3200 Å) or *UVW2* (1800–2250 Å) filter.

Suzaku observed Mrk 79 on 2007 April 3. The two front-illuminated (FI) CCDs (XIS0 and XIS3), the back-illuminated CCD (XIS1) and the HXD-PIN all functioned normally and collected data during this period. The target was observed in the XIS-nominal position.

Cleaned event files from version 2 processed data were used in the analysis and data products were extracted using *XSELECT*. For each XIS chip, source counts were extracted from a 4-arcmin circular region centred on the target. Background counts were taken from surrounding regions on the chip. Response files (*rmf* and *arf*) were generated using *xismfgen* and *xissimarfgen*. A spectrum of the ^{55}Fe calibration source was extracted from each CCD. The Mn $K\alpha$ line was fitted with a Gaussian profile to measure the peak energy. The energies were within 0.2 per cent of the expected value (5.895 keV) and consistent with the current accuracy of the XIS energy scale.¹ After examining for consistency, the data from the XIS-FI were combined to create a single spectrum.

The PIN spectrum was extracted from the HXD data following standard procedures. A non-X-ray background (NXB) file corresponding to the observation was obtained to generate good-time interval (GTI) common to the data and NXB. The data were also corrected for detector deadtime. The resulting PIN exposure was 81 ks. The cosmic X-ray background (CXB) was modelled using the flat response files provided. The CXB and NXB background files were combined to create the PIN background spectrum. In comparison to the source plus background PIN data, Mrk 79 is detected between 12 and 25 keV.

For the X-ray spectral analysis, the source spectra are grouped such that each bin contains at least 20 counts (typically more). For display purposes, data are presented in larger bins. Spectral fitting was performed using *XSPEC* v12.5.0 (Arnaud 1996).

¹ http://www.astro.isas.jaxa.jp/suzaku/doc/suzaku_td/

All parameters are reported in the rest frame of the source unless specified otherwise. The quoted errors on the model parameters correspond to a 90 per cent confidence level for one interesting parameter (i.e. a $\Delta\chi^2 = 2.7$ criterion). We note that the uncertainties in Section 6 (Table 4 later) are underestimated. Given the complexity and slow-fitting nature in the presented model, the uncertainties on any one model parameter are calculated while keeping the other variable parameters fixed. A value for the Galactic column density towards Mrk 79 of $5.27 \times 10^{20} \text{ cm}^{-2}$ (Kalberla et al. 2005) is adopted in all of the spectral fits. Fluxes for all model components are estimated with the *xSPEC* model CFLUX. *K*-corrected luminosities are calculated using a Hubble constant of $H_0 = 70 \text{ km s}^{-1} \text{ Mpc}^{-1}$ and a standard flat cosmology with $\Omega_M = 0.3$ and $\Omega_\Lambda = 0.7$. The *HXD/PIN-XIS* cross-normalization is fixed at 1.16.

3 CHARACTERIZATION OF THE DATA SETS

3.1 X-ray flux and spectral variability

The seven pointed observations were conducted over ~ 7.5 yr and span a range of ~ 3 in broad-band (0.5–10 keV) flux. Between 2003 and 2008, Mrk 79 underwent monitoring on hourly to daily intervals with *RXTE* (Breedt et al. 2009). The pointed observations are compared with the *RXTE* light curve during this campaign (provided courtesy of P. Uttley) to determine what flux state is represented by each observation (Fig. 1). XMM2, XMM6 and SUZ1 are representative of low-flux states, with XMM6 comparable to the lowest states observed with *RXTE*. XMM3 is comparable to a high-flux state though *RXTE* did catch the source about 50 per cent brighter during occasional flaring events. The pointed observations here appear to adequately scrutinize the low-, high- and intermediate-flux states of Mrk 79.

The spectra from the pointed observations are compared in Fig. 2. The spectra appear to harden with decreasing flux, and a narrow emission feature at about 6.4 keV is seen at all epochs. Though the intermediate-flux states (XMM1, XMM4 and XMM5) are very comparable in broad-band flux, there do appear to be some slight changes in the spectral shape.

The light curves from each observation are shown in Fig. 3. Flux variations on the short time-scales (e.g. $\lesssim 1000$ s) probed with

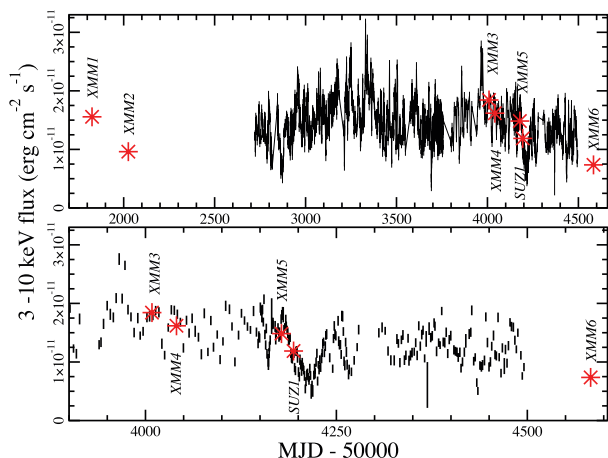


Figure 1. Upper panel: the 3–10 keV long-term *RXTE* light curve is plotted in black. For comparison the 3–10 keV fluxes from each pointed observation are shown as red stars. Lower panel: the light curve from above is enlarged between days 3900–4605 when the pointed observations are more frequent. The pointed observations sample all the typical flux states of Mrk 79.

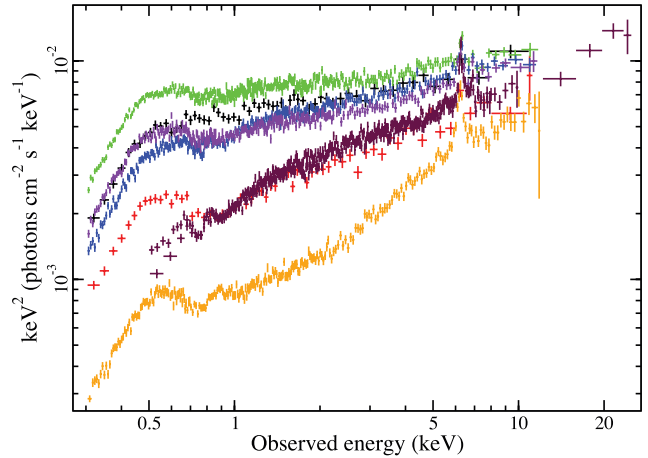


Figure 2. The spectra from all the pointed observations are shown after correcting for the effective area of the detectors. The spectra become progressively harder with decreasing flux. The colour designation is as follows: XMM1 (black), XMM2 (red), XMM3 (green), XMM4 (blue), XMM5 (violet), SUZ1 (maroon) and XMM6 (orange).

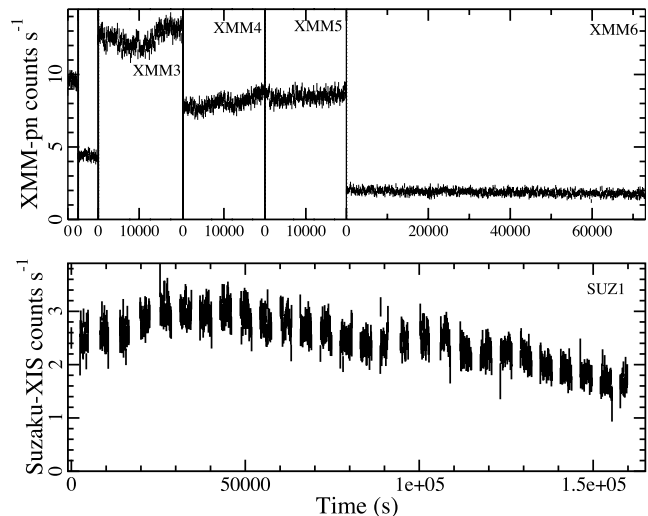


Figure 3. The short-term light curves in 100-s bins from all the pointed observations. All the *XMM-Newton* pn (0.2–12 keV) light curves are presented in the upper panel. Zero marks the start time of each light curve. The count rates and duration of each curve are on comparable scales. XMM1 (leftmost panel) and XMM2 (second panel from left) are short observations (< 10 ks). In the lower panel, the *Suzaku* light curve for the combined XIS in the 0.5–10 keV band is shown. Again, zero marks the start of the observation.

XMM-Newton are present, but are of rather small amplitude. The ~ 2 -d *Suzaku* observation shows larger amplitude variations comparable to the fluctuations measured during the *RXTE* monitoring (Breedt et al. 2009).

Spectral variability is tested for by measuring the fractional variability (F_{var}) at various energies (e.g. Ponti et al. 2004). For observations that were at least 20 ks in duration the F_{var} spectrum is shown in Fig. 4, which confirms the low-amplitude variations seen in the light curves (Fig. 3) and illustrates minimal energy-dependent variability during the *XMM-Newton* observations. Modest spectral variability is observed during the longer *Suzaku* observation as expected since the variability increases with increasing exposure (e.g. Markowitz & Edelson 2004). The amplitude of the variations appears to decrease with increasing energy. Such behaviour has been seen in

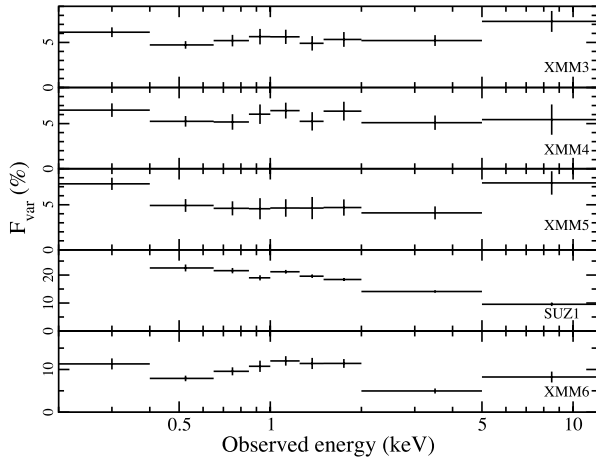


Figure 4. The normalized rms spectrum calculated for observations of at least 20 ks in duration. The *XMM-Newton* and *Suzaku* light curves used are in 750- and 5760-s bins, respectively.

other AGN and attributed to various effects (e.g. changing spectral slope or varying the relative normalization of the continuum components) (e.g. Ponti et al. 2006; Gallo et al. 2007). For our purposes, the detected spectral variability indicates that caution must be exercised when fitting the mean *Suzaku* spectrum.

3.2 Ultraviolet variability

Simultaneous UV photometry with the OM permits examination of the variability at UV wavelengths. The average 2500 Å luminosity over the six *XMM-Newton* observations is $\sim 2.23 \times 10^{28}$ erg s⁻¹ with fluctuations on the ± 10 per cent level (Fig. 5), significantly lower than seen in the X-rays.

The power law between 2500 Å and 2 keV (i.e. α_{ox}) is measured from the simultaneous UV and X-ray observations. According to Just et al. (2007), based on its UV luminosity the expected UV–X-ray slope for Mrk 79 is $\alpha_{\text{ox}}(L_{2500\text{\AA}}) = -1.25 \pm 0.13$. In Fig. 5, $\Delta\alpha_{\text{ox}} = \alpha_{\text{ox}} - \alpha_{\text{ox}}(L_{2500\text{\AA}})$ is plotted for each *XMM-Newton*

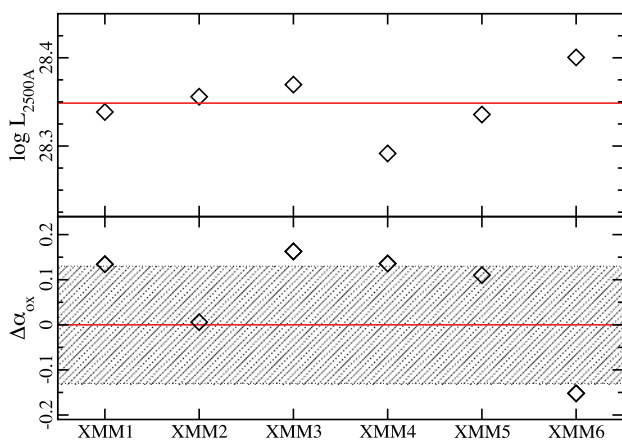


Figure 5. The 2500 Å luminosity (upper panel) and $\Delta\alpha_{\text{ox}}$ (lower panel) is plotted for each *XMM-Newton* observation. The red line in the upper panel identifies the mean UV luminosity. Based on the photometric uncertainties only, the error bars on $\log L_{2500\text{\AA}}$ are comparable to the size of the data points. The red line in the lower panel marks the expected α_{ox} based on the UV luminosity and the shaded region corresponds to the uncertainties in the Just et al. relation. Negative values indicate that the object is X-ray weak compared to the UV luminosity.

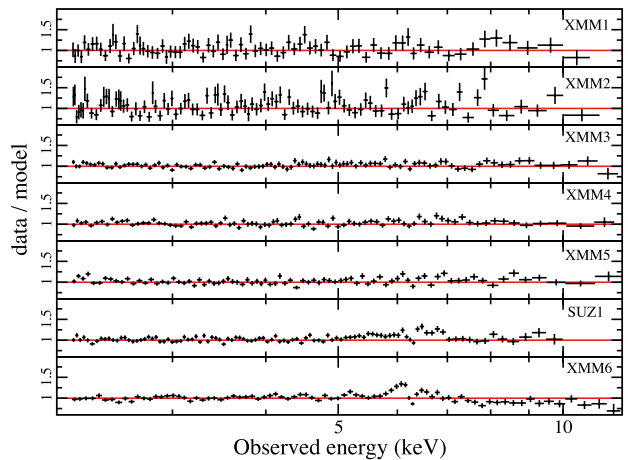
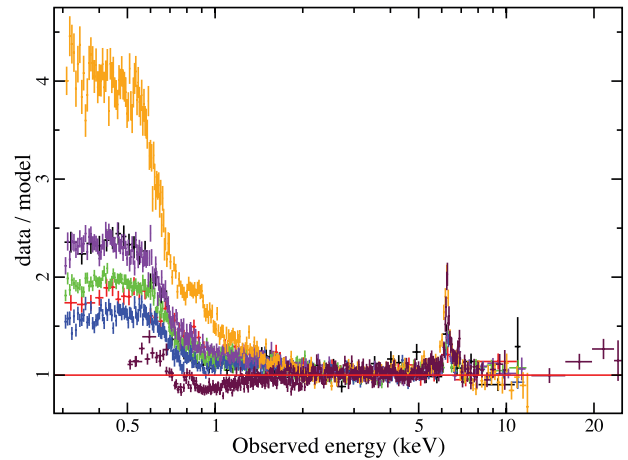


Figure 6. Upper panel: the residuals (data/model) remaining from fitting each spectrum with a power law absorbed by Galactic absorption in the 2.2–4.5 and 7–10 keV bands, and then extrapolating over 0.3–25 keV. A low-energy excess and narrow emission feature at ~ 6.4 keV are present in all spectra. The *Suzaku* data show an excess above 12 keV. Colours are as described in Fig. 2. Lower panel: the residuals of a power law plus narrow Gaussian profile fit to the 2.2–12 keV band. Excess residuals redwards of 6.4 keV are seen in SUZ1 and XMM6.

observation to illustrate the deviation of α_{ox} from the expected value for Mrk 79 based on its 2500 Å luminosity at the time. Most of the time, Mrk 79 appears to be slightly X-ray strong [$\alpha_{\text{ox}}(L_{2500\text{\AA}}) > 0$]. XMM6 is the only observation in which Mrk 79 is in an X-ray-weak state. According to Gallo (2006), marked spectral complexity above 2 keV (i.e. significant deviations from a power law) should be present, which is consistent with Fig. 6. Though the UV luminosity is variable, the plunge into an X-ray-weak state during XMM6 is driven by X-ray variability.

3.3 Phenomenological spectral fits

Fitting a power law to each spectrum in the 2.2–4.5 and 7–10 keV bands and extrapolating over the 0.3–12 keV band (0.5–25 keV for *Suzaku*) reveals a typical Type I AGN spectrum. A soft excess is seen below ~ 2 keV. There is a narrow emission feature at ~ 6.4 keV as well as a slight excess above 10 keV (upper panel of Fig. 6). Qualitatively, the soft excess and the emission feature appear stronger with decreasing flux. The *Suzaku* data only extend down to 0.5 keV and do not show the full extent of the low-energy excess.

The narrow emission feature at ~ 6.4 keV is most likely attributed to Fe K α emission from material distant from the black hole. The spectra above 2.2 keV were refitted with a power law and narrow Gaussian profile revealing the residual in the lower panel of Fig. 6. For XMM1, XMM2, XMM3, XMM4 and XMM5, the simple fit appears to be acceptable. For SUZ1 and XMM6, positive residuals remain redwards of 6.4 keV that could be interpreted as broadened Fe K α emission from the accretion disc. For SUZ1, a second Gaussian profile with a peak energy of 6.46 ± 0.14 keV (6.36 ± 0.02 keV for XMM6) and width of $\sigma = 556^{+123}_{-192}$ eV (142^{+35}_{-18} eV for XMM6) can characterize the residuals. We make note of positive residuals extending down to ~ 4.5 keV in XMM3 but do not consider these as sufficient evidence for an additional component.

Gallo et al. (2006) successfully fitted the snap-shot observations of Mrk 79 (XMM1 and XMM2) with the traditional phenomenological model of a blackbody and power-law continuum, with a high-energy Gaussian profile and low-energy absorption edge. Applying this model to the spectrum at each epoch resulted in reasonably good fits ($\chi^2_{\nu} = 0.89\text{--}1.13$).

The soft excess in Mrk 79 can be parametrized as a blackbody with a varying temperature in the range of 100–140 eV, as typically seen in unabsorbed AGN (e.g. Gierlinski & Done 2004; Crummy et al. 2006). The measured temperature is not correlated with the source luminosity in any obvious way and does not follow the expected $L \propto T^4$ relation attributed to a standard accretion disc of a constant area (Fig. 7). The expected temperature for a standard accretion disc around Mrk 79, assuming a black hole mass of $5.24 \times 10^7 M_{\odot}$ (Peterson et al. 2004) and $L/L_{\text{Edd}} \approx 0.09$ (following Kaspi et al. 2000), peaks at ~ 15 eV. Given the high temperature predicted by the model and apparent variability, a blackbody does not provide a physical description for the soft excess in Mrk 79.

A narrow Gaussian profile is a rational addition evident from the residuals in Fig. 6. The energy is consistent with neutral Fe K α emission and the flux of the line is comparable within uncertainties at all epochs. The average linewidth corresponds to a full width at half-maximum velocity of $\sim 11\,000$ km s $^{-1}$, about twice as high as that measured for H β from the broad-line region (BLR; Peterson et al. 1998). This suggests that the dominant component of the Fe K α emission in Mrk 79 is not coming from a distant torus, but is more likely emission from the accretion disc and the inner BLR.

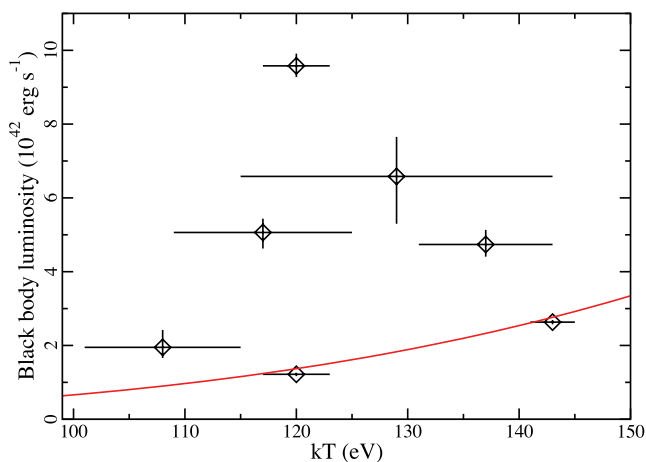


Figure 7. The measured blackbody luminosity and temperature are plotted for each spectrum. The red curve is the fitted $L \propto T^4$ relation (leaving only the normalization free), which clearly does not describe the data.

The best-fitting absorption edge energy at most epochs is ~ 720 eV (673 ± 6 eV for XMM6), and the depth of the feature differs at each epoch. The energy is lower than expected from O VII (739 eV) and not likely associated with absorption by hot local gas (McKernan et al. 2004) since the implied velocities would be higher than the recessional velocity of the AGN. A more physical treatment is required to interpret this component of the spectrum (see Section 6).

4 THE RGS SPECTRUM

The RGS data were reduced using SAS v9.0 (Gabriel et al. 2003) and the most updated calibration files available at the date the reduction was performed (2009 October). The data reduction followed standard procedures as in, for example, Guainazzi & Bianchi (2007). The total number of background-subtracted counts in the nominal RGS energy bandpass (0.3–2 keV) is 674 ± 19 and 727 ± 18 in RGS1 and RGS2, respectively.

Visual inspection of the RGS spectrum does not show the high EW lines typically observed in the high-resolution spectra of highly obscured AGN (cf. Kinkhabwala et al. 2002, and references therein). The statistics of the data does not warrant detailed spectral fitting with physical models. We have therefore limited ourselves to phenomenological simultaneous fits of the combined time-averaged RGS1 and RGS2 spectra.

First, we have performed a blind search for absorption lines. The spectra were fitted in 100-channel intervals with a power-law continuum, photoelectrically absorbed by a column density held fixed to the value due to intervening gas in our Galaxy. At the 90 per cent confidence level for one interesting parameter only one line is detected, with centroid energy $E_c = 698.2 \pm 1.2$ eV and intensity $I = -2.5^{+2.4}_{-2.0} \times 10^{-5}$ cm $^{-2}$ s $^{-2}$. The difference in Cash statistics between a fit with the continuum only and the fit after the inclusion of this absorption line is $\Delta C = 26.1$. The ΔC corresponding to the quoted confidence level is calculated by dividing the distribution percentage point probability by the number of trials, in this case the number of RGS spectral bins (3400), under the approximation that they are independent (this is largely valid for high-resolution cameras) (Svoboda, Guainazzi & Karas 2010). There is no obvious identification for this feature. The nominal closest transition according to the ATOMDB data base would be a resonant transition between the ground state and the $1s4p\ ^1P_1$ electronic configuration of O VII. Given the lack of other detected transitions which could provide information on the velocity shift of the absorbing gas, as well as the modest statistical significance of these detections, we consider it as tentative only. We therefore do not discuss it further.

On the other hand, several emission lines are detected once a similar search procedure as described in Guainazzi & Bianchi (2007) is applied to the combined time-averaged RGS spectra of Mrk 79. Most of them are associated with the N VI and O VII triplets. The centroid energies of the triplet forbidden components are 431 ± 3 and 574 ± 4 eV, respectively. The intensity of the triplet components is reported in Table 2, together with the values of the R , L and

Table 2. Intensities (in units of 10^{-5} cm $^{-2}$ s $^{-1}$) and values of the R , L and G diagnostic parameters for the N VI and the O VII triplets in the time-averaged Mrk 79 RGS spectra.

Species	$I(f)$	$I(i)$	$I(r)$	R	L	G
N VI	2.5 ± 1.5	<2.5	1.4 ± 1.3	>1.0	<3.8	<4.6
O VII	4.9 ± 1.4	<1.8	<0.7	>2.1	–	–

G diagnostic parameters (Porquet & Dubau 2000; Porter & Ferland 2007). The $O\text{VII}$ $H\beta$ is also detected: $E_c = 671_{-5}^{+2}$ eV, $I = 1.7 \pm 0.8 \times 10^{-5} \text{ cm}^{-1} \text{ s}^{-2}$, while the detection of the $O\text{VIII}$ $\text{Ly}\alpha$ is only marginal (i.e. lower than the 90 per cent confidence level).

The values of the R and G parameters, as well as the high intensity ratio between the forbidden components of the $O\text{VII}$ triplet to the $O\text{VIII}$ $\text{Ly}\alpha$ (4.4 ± 3.3 ; Guinazzi et al. 2009), indicate photoionization as the most likely source of ionization for the gas responsible for the emission features. The properties of the photoionized plasma are, however, only poorly constrained: $n_e < 10^{10} \text{ cm}^{-3}$, $T < 10^5 \text{ K}$, $N_{\text{H}} > 10^{20} \text{ cm}^{-2}$. These values are consistent with those typically measured from large-scale photoionized plasmas in obscured AGN (Sako et al. 2000; Kinkhabwala et al. 2002; Armentrout, Kraemer & Turner 2007; Awaki et al. 2008).

5 THE 3–12 keV BAND

5.1 The existence of a broad line

Fig. 6 shows excess residuals in XMM6 and SUZ1 redwards of 6.4 keV that could be described by relativistically broadened iron emission. When fitting broad-band continuum models such as REFLIONX (Ross & Fabian 2005) to the 0.3–12 keV range, the fit will be driven by the soft excess since the statistics are highest below 2 keV. Thus, the reflection and blurring model parameters depend on the interpretation for the soft excess. Here, only the spectrum above 3 keV is examined for the existence of broadened iron emission. Furthermore, only SUZ1 and XMM6 considered as residuals that can be described with a broad Gaussian profile (Section 3.3) are clearly seen at those epochs. This enhances the potential to distinguish the power-law continuum and reflection component.

Initially, the power-law component is replaced with PEXRAV (Magdziarz & Zdziarski 1995) to describe the reflection of an exponential cut-off power law from a neutral disc. The model does not include an emission line, which is inserted separately. According to the best-fitting equivalent width (EW) measurements of the narrow Fe $K\alpha$ line at each epoch, the reflection fraction ($R = \text{EW}/180 \text{ eV}$; George & Fabian 1991) is set to 0.58 and 0.89 for SUZ1 and XMM6, respectively. In addition, two narrow Gaussian profiles representing Fe $K\alpha$ and Fe $K\beta$ are included at fixed energies and relative normalizations (Fe $K\beta = 0.17$ Fe $K\alpha$). The model is statistically acceptable ($\chi^2_{\nu}/\text{d.o.f.} = 0.950/2007$) and fits the narrow core seen in Fig. 6 (upper panel), but leaves broad residuals at both epochs (upper panel of Fig. 8). Two additional Gaussian profiles corresponding to Fe XXV and Fe XXVI are included, but do not improve the fit or residuals significantly (middle panel Fig. 8). In addition, the flux of Fe XXVI is consistent with zero in XMM6.

Replacing the two high-ionization lines with a single Laor profile (Laor 1991) improves the residuals significantly (lower panel of Fig. 8). The number of free parameters is the same as in the model with high-ionization lines since only the energy and normalization are free to vary. The best-fitting energies are $6.60 \pm 0.08 \text{ keV}$ (SUZ1) and $6.35 \pm 0.04 \text{ keV}$ (XMM6).

In a second fitting attempt with the Laor model, the disc inclination (i) and inner disc radius (R_{in}) are allowed to vary, and the emissivity index (α) remains fixed. This is done in order to estimate some of the parameters for when more complicated models are attempted (see Section 6). The derived fit parameters are shown in Table 3. The differing line energies at each epoch could be suggestive of a change in disc ionization. These preliminary fits argue against a maximally rotating black hole in Mrk 79 since $R_{\text{in}} > 1.2 r_{\text{g}}$ (where $1 r_{\text{g}} = GM/c^2$).

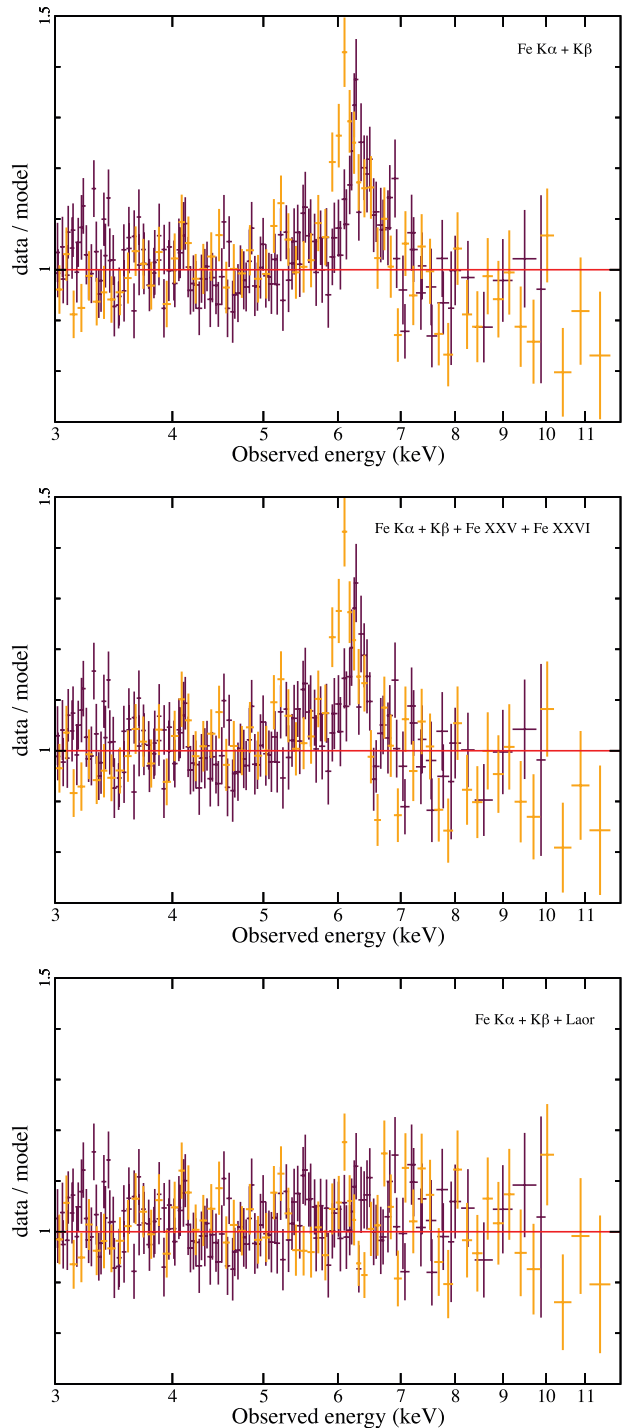


Figure 8. The residuals (data/model) remaining from fitting the XMM6 (orange) and SUZ1 (maroon) spectra between 3 and 12 keV with a PEXRAV continuum and line models as indicated in each panel (see the text for details).

Alternatively, the 3–12 keV spectra are fitted using a power law for the intrinsic continuum and REFLIONX for the reflection component. Blurring of the spectrum, which is thought to originate close to the black hole, is accomplished with KERRCONV (Brenneman & Reynolds 2006). In this case, the blurring and reflection parameters – inclination (i), iron abundance (A_{Fe}), black hole spin (a), outer disc radius (R_{out}) – are not expected to vary significantly between

Table 3. Parameter values for relativistic broad-line (Laor profile) fits to SUZ1 and XMM6. Values that are linked between epochs appear in only one column. Flux units are $\text{erg cm}^{-2} \text{s}^{-1}$. The *f* superscript identifies fixed parameters.

Parameter	SUZ1	XMM6
E_{rest} (keV)	6.77 ± 0.12	6.47 ± 0.10
α	3^f	
R_{in} (r_g)	$6.23^{+1.94}_{-1.12}$	
R_{out} (r_g)	400^f	
i ($^\circ$)	21^{+4}_{-3}	
$\log F_{0.5-10 \text{ keV}}$	$-12.63^{+0.08}_{-0.10}$	$-12.52^{+0.05}_{-0.06}$

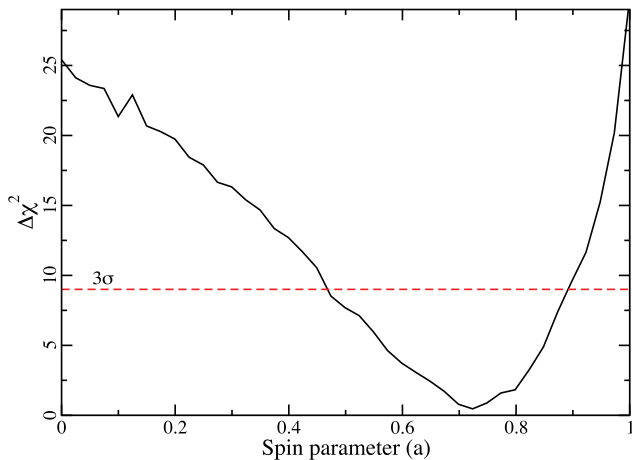


Figure 9. The quality of the fit is tested against the black hole spin parameter showing that extreme (high and low) spin values are discriminated against. The minimum $\Delta\chi^2$ is at $a \approx 0.7$. The red dashed line marks the 3σ level.

the two observations; hence, they are linked. The power-law continuum (Γ and normalization) as well as the ionization parameter and normalization of the reflector are permitted to vary. The quality of fit is equivalent to the Laor model [$\chi^2_{\nu}/\text{degrees of freedom (d.o.f.)} = 0.836/2005$], but provides a more realistic interpretation for the data. The measured spin parameter is $a = 0.7 \pm 0.1$. In Fig. 9, variations in the quality of the 3–12 keV band fit associated with the spin parameter are plotted for the model described. Moderately high spin values ($a \sim 0.40\text{--}0.85$) are favoured. We also examine the influence of iron abundance on the spin parameter. In Fig. 10, the uncertainties in iron abundance and spin value are plotted together showing that they influence each other rather modestly.

5.2 Consideration of absorption models

Miller et al. (2007, 2009b) have described AGN X-ray spectra as being shaped by a composition of ionized absorbers partially covering the primary source. In doing so, their model diminishes the necessity of a very broad relativistic iron line in some cases. The addition of either one or two ionized absorbers to modify the continuum of Mrk 79 produces an equally good fit as the models described above. The appearance of the emission feature is reduced, but not dismissed (Fig. 11). The addition of a Gaussian or Laor profile improves the residuals. In terms of a Gaussian profile, the best-fitting parameters for the SUZ1 and XMM6 data are, respectively, $E = 6.54 \pm 0.08$ and 6.34 ± 0.04 keV; $\sigma = 171^{+60}_{-81}$ and 199^{+43}_{-30} eV; and flux $F = 1.23 \pm 0.04$ and $2.93 \pm 0.03 \times 10^{-13} \text{ erg cm}^{-2} \text{ s}^{-1}$.

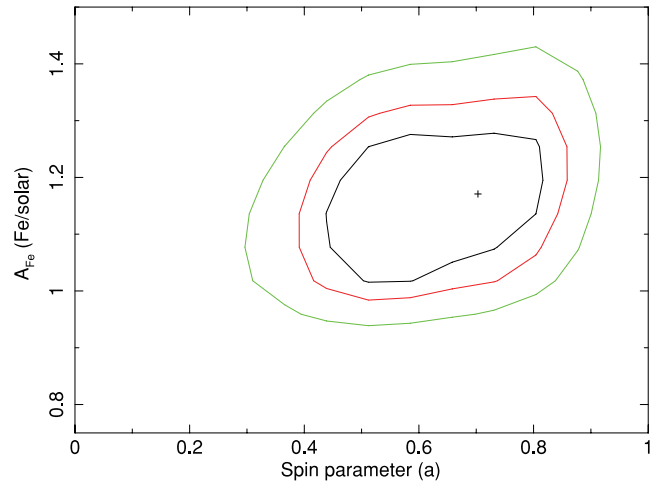


Figure 10. The $\Delta\chi^2 = 2.30, 4.61, 9.21$ contours between iron abundance and black hole spin.

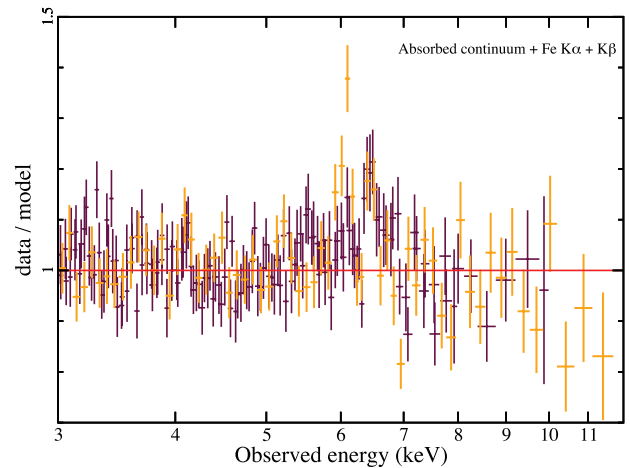


Figure 11. The residuals (data/model) remaining from fitting the XMM6 (orange) and SUZ1 (maroon) spectra between 3 and 12 keV with ionized partial covering continuum and line models as indicated (see the text for details).

6 A MULTI-EPOCH SELF-CONSISTENT MODEL FOR Mrk 79

The above analysis demonstrates that the spectra of Mrk 79 are rather complex and a composition of multiple effects. In this section, we will treat each phenomenon with more physical models while attempting to fit the data from all epochs together. The broadband, multi-epoch analysis is driven by the findings in the previous sections.

6.1 The baseline model: ionized disc reflection

The positive residuals above a power-law continuum between 6 and 7 keV seen in the low-flux states can be attributed to broadened Fe $K\alpha$ emission from the accretion disc near the black hole. This is typically the strongest signature of reflection in AGN X-ray spectra (e.g. Miller 2007). Partial covering models can also describe the continuum in the low-flux states, but do not eliminate the residuals and consequently require a second component.

Illumination of a modestly ionized accretion disc by a power-law continuum source will also generate fluorescence of low-ionization species (e.g. Fe $L\alpha$; Fabian et al. 2009; Zoghbi et al. 2010) below ~ 2 keV (Ballantyne, Ross & Fabian 2001; Ross & Fabian 2005). Once blurred for relativistic effects close to the black hole, it is shown that the low-energy reflection component can mimic the blackbody-like soft excess seen in most Type I AGN (e.g. Crummy et al. 2006).

As a starting point for fitting all the Mrk 79 spectra, the power law plus REFLIONX model used to fit the 3–12 keV band during the low-flux states (i.e. XMM6 and SUZ1, see Section 5) is applied to the broad-band spectrum at all flux states. Even though a prominent broad line is not obvious in the high-flux state spectra, expectations are that a reflection component is still present (i.e. the power-law source still illuminates the accretion disc) but that its flux is diminished relative to the continuum. As with the analysis in Section 5, KERRCONV is used to blur the reflection component. One advantage of fitting multi-epoch data simultaneously is that parameters not expected to vary on the time-scales probed can be linked. In this case, the reflector and blurring parameters – inclination (i), iron abundance (A_{Fe}), black hole spin (a) and outer disc radius (R_{out}) – are not expected to vary on time-scales of 8 yr; hence, they are linked between all epochs.

At all epochs, the inner disc radius (R_{in}) is assumed to be located at the innermost stable circular orbit (ISCO); hence, it is fixed at $R_{\text{in}} = 1.0 r_{\text{ISCO}}$. Initial fits always place the outer disc radius at large distances, so for simplicity R_{out} is fixed at $100.0 r_{\text{ISCO}}$. The emissivity profile of the disc is a power law in radius [$J(r) \propto r^{-\alpha}$], where $\alpha = 3$ is commensurate with a simple lamp post model. The index is left free to vary at each epoch. Including a different index for the inner and outer portions of the disc (i.e. a broken power-law emissivity profile) was initially considered, but deemed unnecessary. The two indices were usually comparable and/or the break radius separating the inner and outer disc regions was very large (e.g. $\gtrsim 150 r_{\text{g}}$). The spin parameter is fixed to $a = 0.7$, the value calculated when fitting only the low-flux states (Section 5). Likewise, the iron abundance is set to $1.2\times$. This was primarily done to keep from generating arbitrarily high spin values that would artificially smooth the spectrum at low energies (i.e. the soft excess) where statistics are best. The ionization parameter of the disc ($\xi = L_{\text{x}}/nr^2$, where n is the hydrogen number density), power-law continuum (Γ and normalization) and normalization of the reflector are permitted to vary at each epoch.

The blurred reflection and power law serve as a reasonable baseline model for all the spectra ($\chi^2_{\text{v}}/\text{d.o.f.} = 1.247/7425$). It results in the same residuals as found with a blackbody and power law, specifically a narrow emission feature at Fe $K\alpha$ energies and sharp wiggles at lower energies. The residuals in the Fe $K\alpha$ complex are treated by adding two narrow Gaussian profiles to mimic emission. The energy of one Gaussian profile is fixed at 7.058 keV representing emission from Fe $K\beta$. The second Gaussian profile, likely due to distant Fe $K\alpha$ emission, is free to vary in energy, width and normalization. The width of the Fe $K\beta$ profile is linked to the free line. In addition, the flux of the Fe $K\beta$ line is constrained to be 0.17 times that of Fe $K\alpha$. Narrow emission lines from highly ionized species of iron (Fe xxv and Fe xxvi) were considered unnecessary in Section 5 and consequently not modelled here. However, the residuals of each spectrum are examined for possible features. The normalization of the Fe $K\alpha$ line is linked between all the spectra as there was no indication of it being variable from one epoch to another (see Section 3.3). In total, the addition of two Gaussian profiles accounts for extra three parameters in the fit.

6.2 The photoionized emitter and warm absorber

The RGS analysis in Section 4 reveals possible absorption, but predominantly emission, from an ionized plasma. The dominance of the forbidden component in the O VII triplet and high O VII (f)/O VIII $L\alpha$ points to photoionization as the primary source of ionization. The XSTAR (Kallman et al. 1996) analytical models WARMABS and PHOTEMIS are used to model the warm absorption and thermal (i.e. recombination and collisional excitation) emission, respectively. The ionized plasma is assumed to have a density of 10^4 cm^{-3} consistent with the density estimated in the RGS analysis. Element abundances were frozen at solar values. The absorber is assumed to cover the power-law and reflection components.

There is significant freedom in how the ionized plasma is modelled at each epoch, and different approaches are considered here. For starters, the parameters of the photoionized emitter are linked between all epochs. One possibility to handle the absorber is to link the column density at all epochs and allow only the ionization to vary. This is a considerable improvement over the baseline model discussed above ($\chi^2_{\text{v}}/\text{d.o.f.} = 1.028/7412$). Statistically, a better quality of fit is achieved when the ionization of the absorber is linked and the column density is free to vary at each epoch ($\Delta\chi^2 = -84$ for the same number of variables). However, in both cases sharp residuals remain at low energies in some spectra. Allowing both the column density and ionization to vary at each epoch is a significant improvement over fits where only one of the parameters is free to vary ($\Delta\chi^2 = 78$ for seven additional free parameters). In addition, the residuals at low energies are also improved ($\chi^2_{\text{v}}/\text{d.o.f.} = 1.006/7406$). Allowing the photoionized emitter to vary in ionization and normalization at each epoch is only a marginal improvement to the fit ($\chi^2_{\text{v}}/\text{d.o.f.} = 0.999/7394$). However, it is physically feasible for the emitter to vary on such time-scales and since the absorber is permitted to vary this is a consistent approach.

The described model produces an acceptable fit to the multi-epoch spectra of Mrk 79 ($\chi^2_{\text{v}}/\text{d.o.f.} = 0.999/7394$). In Fig. 12, the model used to fit the intermediate-flux state of Mrk 79 (XMM1) is shown as well as the residuals resulting from the fit for each spectrum. XMM3, XMM4 and XMM5 benefit from simultaneous *RXTE* observations in which a 10–20 keV flux could be measured. These points are included in Fig. 12 (blue diamonds) to show the very good agreement between the model-predicted flux and the measured flux, but they were not fitted. The model parameters at each epoch are presented in Table 4. We reiterate that parameter uncertainties will be underestimated in this section. Given the complexity of the model, when calculating uncertainties for a given parameter, the other variables were held fixed. Consequently, the variability in a given parameter from one epoch to the next is not as significant as it appears, and examining general trends in the variations is perhaps more valuable.

A complexity that arises in accepting the parameter uncertainties at face value is that the model predicts an apparent correlation between the power-law flux and photon index, in the sense that the intrinsic spectra are harder in the low-flux states. This prediction is different from the general interpretation of reflection or absorption models where the intrinsic slope is constant, but the apparent slope changes due to varying contributions of the separate components. We reconsider the error estimation for Γ in the XMM6 and SUZ1 spectra individually. While maintaining all multi-epoch determined parameters fixed (e.g. inclination, abundances) and varying the remaining parameters, we estimate the more likely uncertainty in Γ at each low-flux state. In both cases, $\Delta\Gamma \approx 0.1$ at a 3σ level. While this alleviates the concern for significant intrinsic power-law shape

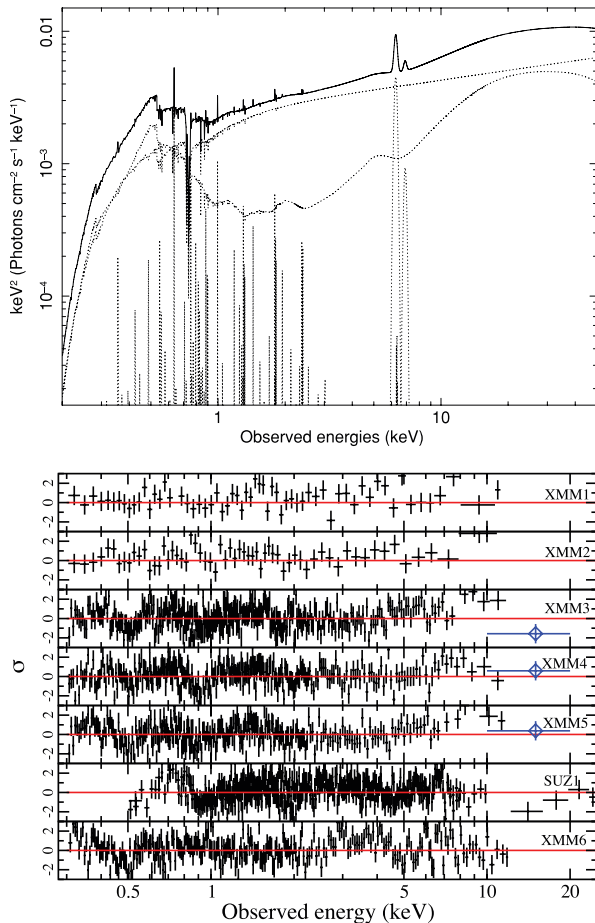


Figure 12. Upper panel: the model used to fit the spectrum of XMM1. XMM1 represents and intermediate flux state for Mrk 79. The model is similar for all the spectra, so only one spectrum is shown for clarity. Lower panel: spectral residuals (in σ) at each observation resulting from the simultaneous multi-epoch fit described in the text and Table 4. The blue diamonds in the residuals are based on simultaneous 10–20 keV flux measured with *RXTE*. They are shown to compare the model-predicted flux above 10 keV with data, but were not part of the fit.

changes during SUZ1, it is still problematic during XMM6. Intrinsic spectral changes in the power-law component are predicted if the primary emission originates from a jet or Comptonization, but the large changes from XMM6 to other epochs are difficult to reconcile.

7 DISCUSSION

7.1 The photoionized plasma

The state of the photoionized emitter and warm absorber shows no correlation with the flux of the power-law emitter (Fig. 13). This alone does not dismiss a connection between the power law and plasma since the sparse data make it impossible to track delays caused by light traveltime effects and recombination time-scales. Of course, the light traveltime delays would be zero for the line-of-sight absorber.

On average, the emitter exhibits a higher ionization parameter than the absorber indicating that they are different structures. If both are ionized by the AGN and have similar densities, then the absorber is the more distant of the two. Using the ionization param-

eter to estimate the distance [$r = (L_x/n\xi)^{1/2}$] between the AGN and absorber places the absorber at $\sim 2 \times 10^{19}$ cm (6.5 pc). The emitter would be approximately half as far from the AGN. Both are too distant from the AGN to detect correlations with AGN luminosity from our data.

The ionization parameter of the emitter is comparable at all epochs except for the lowest flux state (XMM6) where the level of ionization decreases. It is not possible to determine if this change is driven by some prolonged decrease in the continuum flux of the AGN at some point in the past. The emitter shows no significant changes in flux level.

The column density of the near-neutral warm absorber is on the order of 10^{21} cm $^{-2}$, comparable to hydrogen column densities seen in our own Galaxy and could be attributed to a similar structure in Mrk 79. The column density does exhibit some variability (~ 20 per cent). Such variations are not very common in Type I AGN but have been reported previously (e.g. Gallo et al. 2007).

7.2 Bulk motion of the primary source and the role of light bending in Mrk 79

Objects such as IRAS 13224–3809 and 1H 0707–495, where light bending is attributed with a substantial role, often exhibit high values for the emissivity index (e.g. $\alpha > 6$) (e.g. Ponti et al. 2010; Zoghbi et al. 2010), indicating X-ray emission originating from a centrally compact region. In Mrk 79, the best-fitting model was achieved when disc emission over a large area was allowed. This is evident by the relatively shallow emissivity profile measured for the disc. The emissivity index in Mrk 79 is typically between $\alpha \approx 3$ and 5, and this may even be slightly overestimated since, in general, limb-brightening effects are not considered in our blurring model (Svoboda et al. 2009). The emissivity in Mrk 79 is commensurate with a simple lamp post model ($\alpha = 3$).

In the light bending model, the primary component is normally perceived as an isotropic and relatively constant emitter. The observed rapid variability, as described by Miniutti & Fabian (2004), is driven by changes in the distance of the primary emitter from the black hole/accretion disc. The model makes specific predictions on the temporal behaviour of the reflection and power-law components. For example, variations in the two components are correlated when the illuminating source is within a few r_g of the black hole. At intermediate distances ($\sim 10 r_g$), the reflection component remains rather constant while the power law can vary significantly. On long time-scales, as observed in this work, the power-law and reflection components will be largely correlated assuming that the illuminating component is emitting isotropically. In addition, light bending does not exclude the possibility of long-term intrinsic changes in the flux of the primary emitter. Given that these data span nearly 8 yr, long-term intrinsic changes could take place as well. In Fig. 14, average flux values for each observation are plotted for the reflection and power-law components. The figure points to variations of similar amplitude in both components. There is a common trend between the fluxes of the power law and reflection but not a one-to-one correlation.

More importantly, the relative contribution of the reflection component in Mrk 79 is small. We estimated the reflection fraction (R) by comparing *PEXRAV* with simulations of the spectral models above 10 keV at each epoch. The power-law slope, abundances and inclination are fixed to the values derived with the fits (Table 4). The cut-off energy is fixed at 350 keV, the value used by *REFLIONX*. At all epochs the reflection fraction was between $R \approx 0.24$ and 0.73, with the highest R value occurring for XMM6. Notably, R is

Table 4. Best-fitting model parameters for the multi-epoch modelling of Mrk 79. The model component and model parameter are listed in Columns 1 and 2, respectively. Each subsequent column refers to a specific epoch. The inner (R_{in}) and outer (R_{out}) disc radii are given in units of the radius of marginal stability (r_{MSO}), where we have further assumed that $r_{\text{MSO}} = r_{\text{ISCO}}$. The log of the ionization parameter is shown for both ionized plasmas and the warm absorber column density is in units of $\log(N/10^{22} \text{ cm}^{-2})$. Values that are linked between epochs appear in only one column. The f superscript identifies fixed parameters. Fluxes are corrected for Galactic absorption and are in units of $\text{erg cm}^{-2} \text{ s}^{-1}$.

(1)	(2)	(3)	(4)	(5)	(6)	(7)	(8)	(9)
Model component	Model parameter	XMM1	XMM2	XMM3	XMM4	XMM5	SUZ1	XMM6
Power law	Γ	1.76 ± 0.01	1.95 ± 0.01	2.00 ± 0.01	1.81 ± 0.01	1.86 ± 0.01	1.61 ± 0.01	1.49 ± 0.01
	$\log F_{0.5-10 \text{ keV}}$	-10.835 ± 0.007	-10.498 ± 0.006	-10.440 ± 0.002	-10.526 ± 0.002	-10.593 ± 0.003	-10.712 ± 0.002	-11.164 ± 0.003
Warm absorber	$\log \eta/H$	-0.68 ± 0.03	-0.83 ± 0.03	-1.11 ± 0.02	-1.10 ± 0.02	-1.10 ± 0.02	-0.86 ± 0.02	-1.08 ± 0.06
	$\log \xi$	$1.03^{+0.04}_{-0.07}$	$1.94^{+0.26}_{-0.08}$	0.98 ± 0.04	$0.81^{+0.09}_{-0.04}$	1.00 ± 0.04	$0.93^{+0.08}_{-0.04}$	1.73 ± 0.03
Photoemitter	$\log \xi$	$2.09^{+1.22}_{-0.62}$	$1.03^{+1.00}_{-1.03}$	$2.07^{+0.25}_{-0.09}$	$2.13^{+0.41}_{-0.21}$	$2.08^{+0.25}_{-0.17}$	$2.08^{+0.68}_{-0.21}$	$1.38^{+0.05}_{-0.03}$
	$\log F_{0.5-10 \text{ keV}}$	$-13.03^{+0.26}_{-0.71}$	$-13.00^{+0.37}_{-1.04}$	$-12.97^{+0.21}_{-0.41}$	$-13.16^{+0.25}_{-0.64}$	$-13.09^{+0.23}_{-0.50}$	$-13.43^{+0.28}_{-1.00}$	-12.80 ± 0.03
Narrow lines	$E_{\text{Fe K}\alpha}$ (keV)	6.40 ± 0.01						
	$E_{\text{Fe K}\beta}$ (keV)	7.058^f						
	σ (eV)	99^{+15}_{-9}						
	$\log F_{\text{Fe K}\alpha}$	-12.54 ± 0.03						
Blurring	α	$4.62^{+0.31}_{-0.27}$	$4.16^{+0.51}_{-0.40}$	4.83 ± 0.11	3.78 ± 0.13	5.53 ± 0.13	$3.27^{+0.19}_{-0.17}$	4.13 ± 0.10
	a	0.7^f						
	R_{in}	1.0^f						
	R_{out}	100^f						
Reflection	i ($^\circ$)	24 ± 1						
	ξ (erg cm s^{-1})	179 ± 5	57 ± 4	131 ± 3	130 ± 2	145 ± 2	177 ± 6	60 ± 1
Total flux	A_{Fe} (Fe/solar)	1.2^f						
	$\log F_{0.5-10 \text{ keV}}$	-11.126 ± 0.014	-11.174 ± 0.029	-10.804 ± 0.005	-11.154 ± 0.008	-10.892 ± 0.005	-11.551 ± 0.017	-11.439 ± 0.006
Total flux	$\log F_{0.5-10 \text{ keV}}$	-10.733 ± 0.005	-10.445 ± 0.005	-10.354 ± 0.001	-10.470 ± 0.002	-10.492 ± 0.002	-10.674 ± 0.002	-10.962 ± 0.002
	$\log F_{2-10 \text{ keV}}$	-10.929 ± 0.005	-10.701 ± 0.005	-10.631 ± 0.001	-10.687 ± 0.002	-10.736 ± 0.002	-10.834 ± 0.002	-11.083 ± 0.002

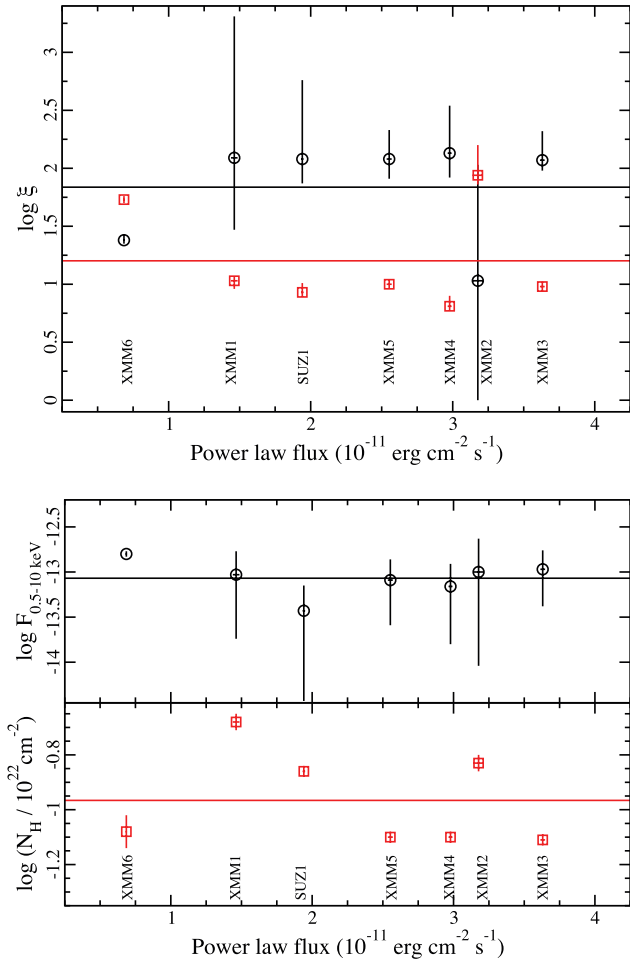


Figure 13. Upper panel: the logarithm of the ionization parameter of the photoionized emitter (black circles) and absorber (red squares) is plotted against the flux of the power-law component. The average ionization parameters for each component are also shown (straight lines). Lower panel: the 0.5–10 keV flux of the emitter (black circles) and column density of the absorber (red squares) is shown against the power-law flux. Uncertainties are plotted on all quantities, but may be smaller than the data point itself.

variable from epoch to epoch and is consistently less than 1. While reflection features are present in Mrk 79, light bending does not appear to be a significant factor.

The variations in R also advocate a non-standard geometry for the illuminating source. If the source were simply varying its luminosity to produce the observed variability, there should exist a good correlation between the reflection and power-law flux along with a constant reflection fraction. This is not the case. The basic picture of variability in which the primary source, wherever it is located, only varying in luminosity with its other characteristics is challenged.

One can imagine a situation in which a compact primary source is located at a few r_g , hence subject to general relativistic effects, but is moving away at mildly relativistic speeds (e.g. Reynolds & Fabian 1997; Beloborodov 1999). Beloborodov proposed such a model to explain the low reflection fraction in the black hole binary Cyg X-1. Beloborodov described the nature of the primary source as an active corona atop the accretion disc. The plasma in the active regions is heated by magnetic flares, and it can be ejected at mildly relativistic velocities if the blob is dominated by e^\pm pairs. As a consequence of beaming, the reflection fraction is reduced even in the presence of light bending effects. From equation (3) of

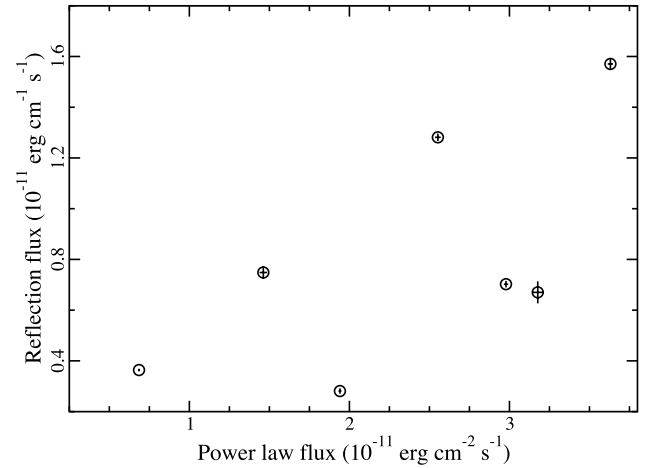


Figure 14. The 0.5–10 keV unabsorbed flux of the reflection and power-law components is plotted. Variability of similar amplitude is present in both.

Beloborodov (1999), $R = (1 - \beta/2)(1 - \beta \cos i)^3 / (1 + \beta)^2$, the bulk velocity of the illuminating blob ($\beta = v/c$) is related to R , where i is the inclination of the system. We determine β at each epoch from the estimated reflection fraction. The maximum velocity will occur at the lowest R (≈ 0.24) and in this case is $\beta \approx 0.32$. As the source is radio-quiet, one would not expect these ejections to escape. For the estimated β , the escape radius from the $5.24 \times 10^7 M_\odot$ black hole in Mrk 79 is $\approx 20 r_g$. For higher values of R , one can allow for smaller β , which would result in sources within an even larger distance. Light bending could have a diminished role in Mrk 79 if the source is dominated by beaming. The fact that Mrk 79 tends to be X-ray strong for its UV luminosity (Fig. 5) is consistent with the X-rays being beamed.

As a consistency check we used equation (10) of Beloborodov, $\Gamma \approx 2[(1 - \beta^2)^{-1/2}(1 + \beta)]^{-0.3}$, to compare the predicted photon index with our measured values (Table 4). There is very good agreement between the measured and predicted Γ (within a few per cent) for the high-flux observations (XMM1–XMM5). For the low-flux observations (SUZ1 and XMM6) the difference is 10–20 per cent, and the $\Gamma(\beta)$ relation for this active corona model cannot alone explain the low-state spectral hardening. As discussed in Section 6, this is more problematic for XMM6. We note that SUZ1 and XMM6 were the longest observations and did exhibit some spectral variability within the observation (Fig. 4) that would affect fitting of the average spectrum.

From long-term optical and X-ray monitoring of Mrk 79, Breedt et al. (2009) found that the optical (V band) and X-ray are highly correlated with a delay of 0_{-4}^{+2} d. Breedt et al. found that the optical variations could still be produced by thermal reprocessing of variable X-rays if the height of the illuminating X-ray source is on the order of $21.5 r_g$. At $\sim 20 r_g$ the light traveltime delay between the illuminating X-ray source and the disc is $\tau = 20 r_g / c = 5000$ s. Consequently, a delay of $\tau \approx 5$ –10 ks between the power-law and reflection components is possibly detectable. Despite all the high-quality data in this study, the XMM1–XMM5 observations last $\lesssim 20$ ks and the *Suzaku* data include gaps in the light curve every ~ 5.6 ks due to its low-Earth orbit rendering them unsuitable to search for a $\gtrsim 5$ -ks lag. Only XMM6 is sufficiently long enough to search for such a lag, and interestingly the cross-correlation between the 0.2–0.8 keV (reflection component) and 1.5–2 keV (power-law component) bands does suggest a shift in the peak to negative times (i.e. high energy leads low-energy changes). However, the XMM6

light curve suffers from the fact that it drops smoothly with time and lacks distinct features to build a correlation on (Fig. 3). Any detection of a lag with this light curve is judged questionable.

Coincidentally, Breedt et al. (2009) found a best-fitting disc inclination of 24° from modelling the long-term multiwavelength light curve. We determine a similar inclination $i = 24 \pm 1^\circ$ in our independent X-ray spectral analysis of the source.

On average, the analysis of Mrk 79 is consistent with the illuminating (power-law) source being beamed and located at large distances ($\gtrsim 20 r_g$) from the disc.

7.3 Limitations in measuring the black hole spin

Data quality and spectral models have reached such sophistication that the black hole spin parameter can now be measured from the broadened Fe $K\alpha$ line in Galactic black holes (e.g. Miller et al. 2009a) and AGN (e.g. Brenneman & Reynolds 2006; Miniutti et al. 2009; Schmoll et al. 2009).

For Mrk 79, a moderately high spin value is measured ($a = 0.7 \pm 0.1$) by modelling only the high-energy spectrum. Under the assumption that the soft excess in AGN is the reflection component, it becomes tempting to use the high signal-to-noise ratio data below 3 keV to constrain black hole spin. In principle this is fine, but one must acknowledge how complicated this spectral region is. In addition to uncertainties in the calibration, there may be unmodelled complexities in the ionized absorber/emitter and in the reflection spectrum itself. These complexities could strongly affect conclusions about spin.

Figs 9 and 10 also seem to exclude the possibility of a maximally spinning black hole. In general, it is also difficult to conclusively exclude extremely high spin values since our models are built under the assumption that the disc is truncated at the ISCO. One cannot exclude the possibility that a system includes a maximal spinning black hole, but that the disc is truncated at a larger radius. The broad line in Mrk 79 is particularly weak (Fig. 8) and could be consistent with emission originating from large radii.

8 CONCLUSIONS

Broad-band X-ray spectra (0.3–25 keV) of the Seyfert 1.2 galaxy Mrk 79 are analysed in an attempt to examine long-term variability. The data are obtained with *XMM-Newton* and *Suzaku* at seven different epochs spanning nearly 8 yr and cover a factor of about 3 in broad-band flux between low- and high-flux states. The short time-scale (i.e. within an observation) flux and spectral variations are typically small, making Mrk 79 useful for studying the long-term spectral variability and ‘average’ spectrum. The main results are as follows.

(1) The multi-epoch, broad-band continuum is consistent with a primary power-law flux component and disc reflection, both modified by absorption and emission from an ionized plasma. The relative weakness of the disc reflection features in these spectra is consistent with a model for stellar-mass black holes wherein the power-law continuum arises in flares that are driven vertically from the disc. Variations in the illuminating and reflected components do not suggest that light bending dominates the observed flux trends.

(2) Under the assumption that the inner disc is truncated at r_{ISCO} , a moderately high black hole spin parameter is found ($a = 0.7 \pm 0.1$).

(3) Low-density, photoionized plasma seen predominately in emission is observed and consistent with arising at large distances

from the black hole. The measured parameter values are consistent with those typically measured from large-scale photoionized plasmas in obscured AGN.

(4) Simultaneous UV photometry was obtained for six of the seven observations. The UV are variable to a lesser degree than the X-rays. Measurements of α_{ox} show that Mrk 79 tends to be in an X-ray-bright state compared to its UV luminosity. This would be consistent with the notion that the X-rays are beamed. Mrk 79 was caught in an X-ray-weak state during only one observation (XMM6) for certain. In the X-ray-weak state, the 2–10 keV spectrum appears harder and deviates significantly from a simple power law.

The modest intra-observation variability exhibited by Mrk 79 introduces the potential to obtain a high signal-to-noise ratio average spectrum of the source. The multi-epoch monitoring allows for several model parameters to be constrained with high precision, allowing for a more accurate determination of the variable components. Mrk 79 does not appear to be a particularly extreme active galaxy, but perhaps it is more representative of a typical AGN, and consequently it is important to scrutinize it. *Astro-H* and International X-ray Observatory will have substantially better energy resolution and hard X-ray sensitive than current X-ray missions, thereby improving our ability to constrain the warm emitter/absorber and reflection component.

ACKNOWLEDGMENTS

The *XMM-Newton* project is an ESA Science Mission with instruments and contributions directly funded by ESA Member States and the USA (NASA). Thanks to Damien Robertson for α_{ox} measurements and Phil Uttley for the *RXTE* light curve.

REFERENCES

- Armentrout B. K., Kraemer S. B., Turner T. J., 2007, *ApJ*, 665, 237
 Arnaud K., 1996, in Jacoby G., Barnes J., eds, *ASP Conf. Ser. Vol. 101*, *Astronomical Data Analysis Software and Systems*. Astron. Soc. Pac., San Francisco, p. 17
 Awaki H. et al., 2008, *PASJ*, 60, S293
 Bachev R., Grupe D., Boeva S., Ovcharov E., Valcheva A., Semkov E., Georgiev Ts., Gallo L. C., 2009, *MNRAS*, 399, 750
 Ballantyne D. R., Ross R. R., Fabian A. C., 2001, *MNRAS*, 327, 10
 Beloborodov A. M., 1999, *MNRAS*, 510, 123
 Breedt E. et al., 2009, *MNRAS*, 394, 427
 Brenneman L. W., Reynolds C. S., 2006, *ApJ*, 652, 1028
 Crummy J., Fabian A., Gallo L., Ross R., 2006, *MNRAS*, 365, 1067
 den Herder J. W. et al., 2001, *A&A*, 365, 7
 Fabian A. C. et al., 2009, *Nat*, 459, 540
 Gabriel C., Denby M., Fyfe D. J., Hoar J., Ibarra A., 2003, in Ohsenbein F., Allen M., Egret D., eds, *ASP Conf. Ser. Vol. 314*, *Astronomical Data Analysis Software and Systems XIII*. Astron. Soc. Pac., San Francisco, p. 759
 Gallo L. C., 2006, *MNRAS*, 368, 479
 Gallo L. C., Tanaka Y., Boller T., Fabian A. C., Vaughan S., Brandt W. N., 2004, *MNRAS*, 353, 1064
 Gallo L. C., Fabian A. C., Boller Th., Pietsch W., 2005, *MNRAS*, 363, 64
 Gallo L. C., Lehmann I., Pietsch W., Boller Th., Brinkmann W., Friedrich P., Grupe D., 2006, *MNRAS*, 365, 688
 Gallo L. C., Brandt W. N., Costantini E., Fabian A. C., Iwasawa K., Papadakis I. E., 2007, *MNRAS*, 377, 391
 George I. M., Fabian A. C., 1991, *MNRAS*, 249, 352
 Gierlinski M., Done C., 2004, *MNRAS*, 349, 7
 Grupe D., Komossa S., Gallo L. S., Fabian A. C., Larsson J., Pradhan A. K., Xu D., Miniutti G., 2008, *ApJ*, 681, 982

- Guainazzi M., 2010, XMM–Newton Calibration Documents (CAL-TN-0018)
- Guainazzi M., Bianchi S., 2007, MNRAS, 374, 1290
- Guainazzi M., Risaliti G., Nucita A., Wang J., Bianchi S., Soria R., Zezas A., 2009, A&A, 505, 589
- Iwasawa K., Tanaka Y., Gallo L. C., 2010, A&A, 514, 58
- Jansen F. et al., 2001, A&A, 365, L1
- Just D. W., Brandt W. N., Shemmer O., Steffan A. T., Schneider D. P., Chartas G., Garmire G. P., 2007, ApJ, 665, 1004
- Kalberla P. M. W., Burton W. B., Hardmann D., Arnal E. M., Bajaja E., Morras R., Pöppel W. G. L., 2005, A&A, 440, 775
- Kallman T. R., Liedahl D., Osterheld A., Goldstein W., Kahn S., 1996, ApJ, 465, 994
- Kaspi S., Smith P. S., Netzer H., Maoz D., Jannuzi B. T., Giveon U., 2000, ApJ, 533, 631
- Kinkhabwala A. et al., 2002, ApJ, 575, 732
- Laor A., 1991, ApJ, 376, 90
- Magdziarz P., Zdziarski A. A., 1995, MNRAS, 273, 837
- Markowitz A., Edelson R., 2004, ApJ, 617, 939
- Mason K. O. et al., 2001, A&A, 365, 36
- Miller J. M., 2007, ARA&A, 45, 441
- Miller L., Turner T. J., Reeves J. N., George I. M., Kraemer S. B., Wingert B., 2007, A&A, 463, 131
- Miller J. M., Reynolds C. S., Fabian A. C., Miniutti G., Gallo L. C., 2009a, ApJ, 697, 900
- Miller L., Turner T. J., Reeves J. N., 2009b, MNRAS, 399, 69
- Miniutti G., Fabian A. C., 2004, MNRAS, 349, 1435
- Miniutti G., Panessa F., de Rosa A., Fabian A. C., Malizia A., Molina M., Miller J. M., Vaughan S., 2009, MNRAS, 398, 255
- Mitsuda K. et al., 2007, PASJ, 59S, 1
- Peterson B., Wanders I., Bertram R., Hunley J., Pogge R., Wagner R., 1998, ApJ, 501, 82
- Peterson B. M. et al., 2004, ApJ, 613, 682
- Ponti G., Cappi M., Dadina M., Malaguti G., 2004, A&A, 417, 451
- Ponti G., Miniutti G., Cappi M., Maraschi L., Fabian A. C., Iwasawa K., 2006, MNRAS, 368, 903
- Ponti G. et al., 2010, MNRAS, 406, 2591
- Porquet D., Dubau J., 2000, A&AS, 143, 495
- Porter R. L., Ferland G. L., 2007, ApJ, 664, 586
- Reynolds C. S., Fabian A. C., 1997, MNRAS, 290, L1
- Risaliti G. et al., 2009, ApJ, 696, 160
- Ross R. R., Fabian A. C., 2005, MNRAS, 358, 211
- Sako M., Kahn S. M., Paerels F., Liedahl D. A., 2000, ApJ, 542, 684
- Schmoll S. et al., 2009, ApJ, 703, 2171
- Sobolewska M. A., Papadakis I. E., 2009, MNRAS, 399, 1597
- Strüder L. et al., 2001, A&A, 365, L18
- Svoboda J., Dovčiak M., Goosmann R., Karas V., 2009, A&A, 507, 1
- Svoboda J., Guainazzi M., Karas V., 2010, A&A, 512, 62
- Turner M. J. L. et al., 2001, A&A, 365, 27
- Zoghbi A., Fabian A. C., Uttley P., Miniutti G., Gallo L. C., Reynolds C. S., Miller J. M., Ponti G., 2010, MNRAS, 401, 2419

This paper has been typeset from a $\text{\TeX}/\text{\LaTeX}$ file prepared by the author.